Optical diagnostics of atmospheric pressure air plasmas

C O Laux[1,2], T G Spence[3], C H Kruger and R N Zare[4]

High Temperature Gasdynamics Laboratory, Mechanical Engineering Department,
Stanford University, Stanford, CA 94305, USA

E-mail: christophe.laux@em2c.ecp.fr

Abstract
Atmospheric pressure air plasmas are often thought to be in local
thermodynamic equilibrium owing to fast interspecies collisional exchange
at high pressure. This assumption cannot be relied upon, particularly with
respect to optical diagnostics. Velocity gradients in flowing plasmas and/or
elevated electron temperatures created by electrical discharges can result in
large departures from chemical and thermal equilibrium. This paper reviews
diagnostic techniques based on optical emission spectroscopy and cavity
ring-down spectroscopy that we have found useful for making temperature
and concentration measurements in atmospheric pressure plasmas under
conditions ranging from thermal and chemical equilibrium to
thermochemical nonequilibrium.

Introduction

The techniques described in this paper were applied to
measurements in three types of air or nitrogen plasmas. The
first case [1] corresponds to an air plasma produced by a 50 kW
inductively coupled plasma torch, flowing at a relatively low
velocity ($10 \, \mathrm{m \, s^{-1}}$). In this case, the plasma is close to local
thermodynamic equilibrium (LTE) because the convection
rates are lower than those of chemical reactions, and because
the measurements are made in the field-free region downstream
of the induction coil of the plasma torch. The second case [2]
corresponds to a recombining air or nitrogen plasma flowing
at high velocity ($\sim 1 \, \mathrm{km \, s^{-1}}$) through a water-cooled test-
section. At this velocity, the convective rates are faster than the
rates of chemical reactions and the plasma reaches chemical
nonequilibrium at the test-section exit. No electric field is
applied in these experiments. Therefore, the temperatures
of free-electrons and heavy species remain equilibrated and
the flow is close to thermal equilibrium. The third case

corresponds to glow discharges generated by a DC electric
field in atmospheric pressure air [3]. A characteristic of glow
discharges is that the electron temperature T_e is elevated with
respect to the temperature T_g of heavy species. Representative
conditions are $T_g = 2000 \, \mathrm{K}$ and $T_e = 1 \, \mathrm{eV}$ ($11\,600 \, \mathrm{K}$). Under
these conditions, energetic electrons can cause a significant
degree of dissociation and ionization. These plasmas are
therefore in thermal and chemical nonequilibrium.

In all three cases, it can be assumed that the rotational
temperature is close to the gas temperature because rotational
relaxation is fast at atmospheric pressure. On the other
hand, no simple assumption holds regarding the vibrational
and electronic population distributions. The often-used
assumption that $T_{\mathrm{electronic}}$ and $T_{\mathrm{vibrational}}$ are approximately
equal to the electron temperature is not always valid in
nonequilibrium plasmas. In fact, we have shown [4] that
this assumption is incorrect in nitrogen glow discharges
at atmospheric pressure. Thus, great care must be
exercised in interpreting optical diagnostics in nonequilibrium
flows. Section 2 of this paper presents an overview of
our experimental plasma generation and optical diagnostic
facilities. Section 3 describes the spectroscopic model
employed in our data analyses. Section 4 illustrates three
methods for measuring the rotational temperature in air and
nitrogen plasmas. Section 5 presents optical techniques to
measure the concentration of electrons and N_2^+ ions.

---

[1] Author to whom correspondence should be addressed.
[2] Present address: Ecole Centrale Paris, Laboratoire EM2C, Grande Voie des
Vignes, 92290 Chatenay-Malabry, France.
[3] Present address: Chemistry Department, Loyola University, New Orleans.
[4] Chemistry Department, Stanford University, Stanford, CA 94305, USA.

1. Experimental facilities

The air and nitrogen plasmas investigated in our laboratory are produced with a 50 kW inductively coupled plasma torch operating at 4 MHz. The atmospheric pressure plasmas exit the torch through interchangeable nozzles 1–7 cm in diameter. Figure 1(*a*) shows the torch head and plasma plume for the experiments with slow flowing, LTE air plasmas. Here, the nozzle diameter is 7 cm. Figure 1(*b*) shows the experimental set-up for our recombination studies with air and nitrogen plasmas. The exit nozzle diameter is 1 cm, and water-cooled test-sections of various lengths are placed downstream of the torch in order to force rapid plasma recombination in a well-controlled environment. Finally, figure 1(*c*) shows a photograph of a glow discharge created by applying a DC electric field in a fast flowing ($\sim$450 m s^{-1}), low gas temperature (2200 K), atmospheric pressure air plasma.

Figure 2 shows a schematic of the experimental set-up for optical emission spectroscopy (OES) measurements. The OES measurements presented here were made with a $\frac{3}{4}$-m monochromator fitted with a 2000 × 800 pixel CCD camera (SPEX TE2000) or a photomultiplier tube (Hamamatsu R1104). Absolute calibrations of the spectral intensities were made using radiance standards including a calibrated tungsten strip lamp and a 1 kW argon arc. Second- and higher-order light was rejected with long pass filters. Chromatic aberrations were minimized by using spherical mirrors and/or MgF$_2$ lenses in the optical train.

2. Spectroscopic model

Considerable work has been devoted in our laboratory to the development of spectroscopic models for the interpretation of air plasma diagnostics. The SPECAIR code [5] was developed on the basis of the NonEQuilibrium Air Radiation code (NEQAIR) of Park [6]. The current version of SPECAIR [5] models 37 molecular transitions of NO, N$_2$, N$_2^+$, O$_2$, CN, OH, NH, C$_2$, and CO, as well as atomic lines of N, O, and C. The model provides accurate simulations of the absolute spectral emission and absorption of air from 80 nm to 5.5 μm. As an illustration of the capabilities of the model, figure 3 shows a comparison between *absolute* intensity emission spectra measured in LTE air and SPECAIR predictions. The plasma conditions are those corresponding to the temperature profile of figure 4, with a peak centreline temperature of approximately 7500 K. As can be seen in figure 3, the model is able to reproduce the line positions and intensities of the experimental spectra.

3. Temperature measurements

In LTE plasmas, a single temperature characterizes all internal energy modes (vibrational, rotational and electronic). This temperature can be determined from the absolute intensity of any atomic or molecular feature, or from Boltzmann plots of vibrational or rotational population distributions. Figure 4 shows temperature profiles measured in the air plasma of figure 1(*a*). All spectroscopic measurements were Abel inverted to produce radial temperature profiles [1]. The 'LTE' and Boltzmann temperatures are based on the absolute and relative intensities, respectively, of various atomic lines. The rotational temperature profiles were obtained from measurements of the NO γ (0, 1) band shape, using the technique proposed by Gomès *et al* [7]. The vibrational temperature profile was measured from the relative intensities of the (0, 0) and (2, 1) bandheads of N$_2^+$ B–X (first negative system) at 391.4 nm and 356.4 nm, respectively. As can be seen from figure 4, the measured vibrational, rotational, and electronic temperature profiles are to within experimental uncertainty in good agreement with one another. We conclude that the plasma is close to LTE conditions.

In nonequilibrium plasmas, the techniques described in the foregoing paragraph may not provide reliable information about the gas temperature because of departures from equilibrium in the distribution of internal energy state populations. The gas temperature is then best inferred from the
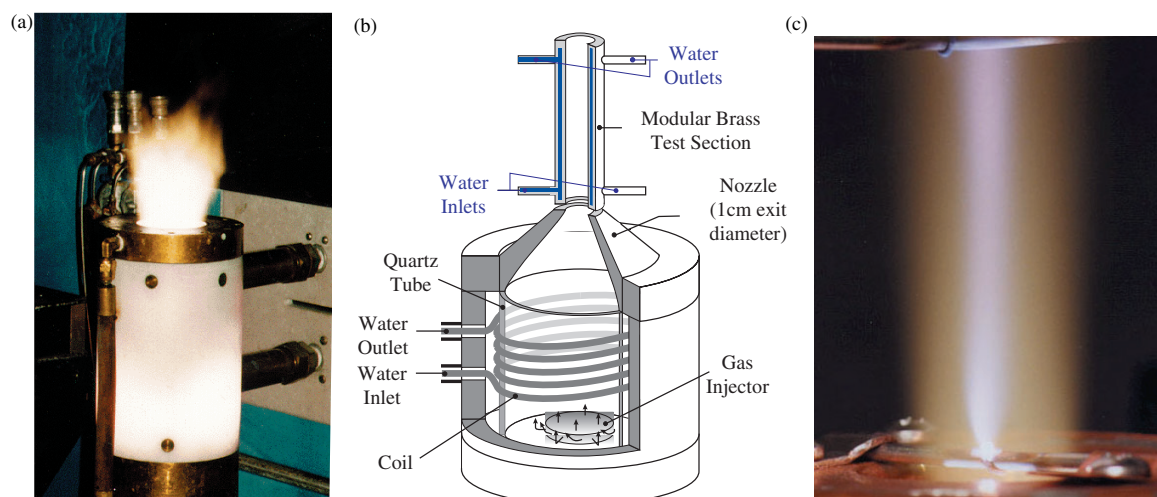

Figure 1. Experimental set-ups for the three cases of interest: (*a*) torch head and plasma plume for LTE air plasma experiments; (*b*) schematic of torch head with nonequilibrium test-section for air and nitrogen recombination experiments; and (*c*) DC glow discharge experiments in air at 2200 K (1.4 kV cm^{-1}, 200 mA). Interelectrode distance = 3.5 cm. The measured electron number density in the bright central region of the discharge is approximately 10^{12} cm^{-3}.
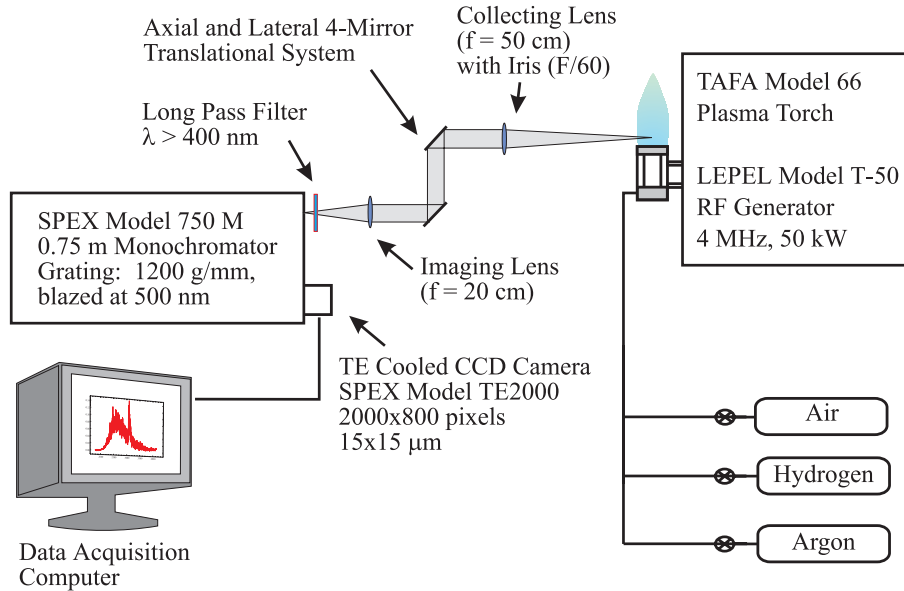
Figure 2. Typical experimental set-up for emission diagnostics.

intensity distribution of rotational lines. Various transitions of O_2, N_2, N_2^+, and NO (dry air) and OH (humid air) can be used, depending on the level of plasma excitation. As an illustration of the numerous emission bands of air species, figure 5 shows the ultraviolet emission spectra of equilibrium, atmospheric pressure air with a water vapour mole fraction of 1.3%, for temperatures in the range 3000–8000 K. Bands of NO, OH, and O_2 dominate the spectrum at temperatures below $\sim$5000 K. The second positive system of N_2 (C–B), the first negative system of N_2^+ (B–X), and atomic lines of O and N appear at higher temperatures. The emission features of figure 5 can also be observed in low temperature nonequilibrium air plasmas with elevated electronic temperature. Such plasmas are readily produced by means of electrical discharges.

In low temperature humid air plasmas, the emission spectrum of the OH A–X transition around 300 nm provides a particularly convenient way to measure the rotational temperature. At higher temperatures, or in the presence of an electric field, the OH transition is overlapped by strong emission from N_2 C–B (second positive system). In this case, the rotational temperature can be measured from N_2 C–B rotational lines. At even higher temperatures or higher electric field excitation, many molecular transitions appear in the spectrum and an accurate spectroscopic model is required to extract individual lines of a particular system. For these conditions, we recently proposed a method based on selected rotational lines of N_2^+ B–X [8]. The OH, N_2, and N_2^+ rotational temperature measurement techniques are described in the following subsections.

3.1. OH A–X rotational temperature measurements

The OH A–X transition is one of most intense systems emitted by low temperature air plasmas containing even a small amount ($\sim$1%) of H_2 or H_2O. The rotational temperature can be obtained by fitting the entire band, or more simply from the relative intensities of two groups of rotational lines corresponding to the R and P branches of

the OH A–X (0, 0) vibrational band. These branches form distinct peaks at about 307 nm and 309 nm, respectively, as shown in figure 6. The spectroscopic model used in SPECAIR for OH A–X is described in [9]. This technique provides a sensitive thermometer because the relative intensity of the two peaks varies rapidly with the rotational temperature (figure 7). Another advantage of the technique is that it does not require absolute or relative intensity calibration because the response of usual detection systems is nearly constant over the small spectral range of interest. However, one should be aware of potential difficulties associated with self-absorption, non-Boltzmann rotational population distribution, and interferences with other species present in the plasma.

3.1.1. Self-absorption. Because the peak of the P-branch is more self-absorbed than the peak of the R-branch, the P/R intensity ratio at a given rotational temperature becomes smaller as the optical thickness of the plasma increases. According to figure 7, a smaller P/R ratio would suggest a rotational temperature higher than its actual value. If the peak of the P branch were self-absorbed by 4% (for instance), the rotational temperature inferred from figure 7 would be approximately 100 K higher than the actual rotational temperature. The optical thickness of the plasma depends on the length L of plasma, the concentration of OH, and the temperature. In equilibrium plasmas, the OH concentration is a function of the temperature, pressure and mole fraction X_{H_2O} of water vapour in the cold air stream. Figure 8 shows the values of the product $X_{H_2O}L$ that would cause 4% of self-absorption at the peak of the P branch. This curve can be used to estimate the importance of self-absorption effects in a particular experimental set-up. In a 1-cm air plasma at 2000 K, for example, self-absorption effects can be neglected if the mole fraction of water vapour is less than about 1%.

3.1.2. Non-Boltzmann rotational distribution. Departures from a rotational Boltzmann distribution may occur as a
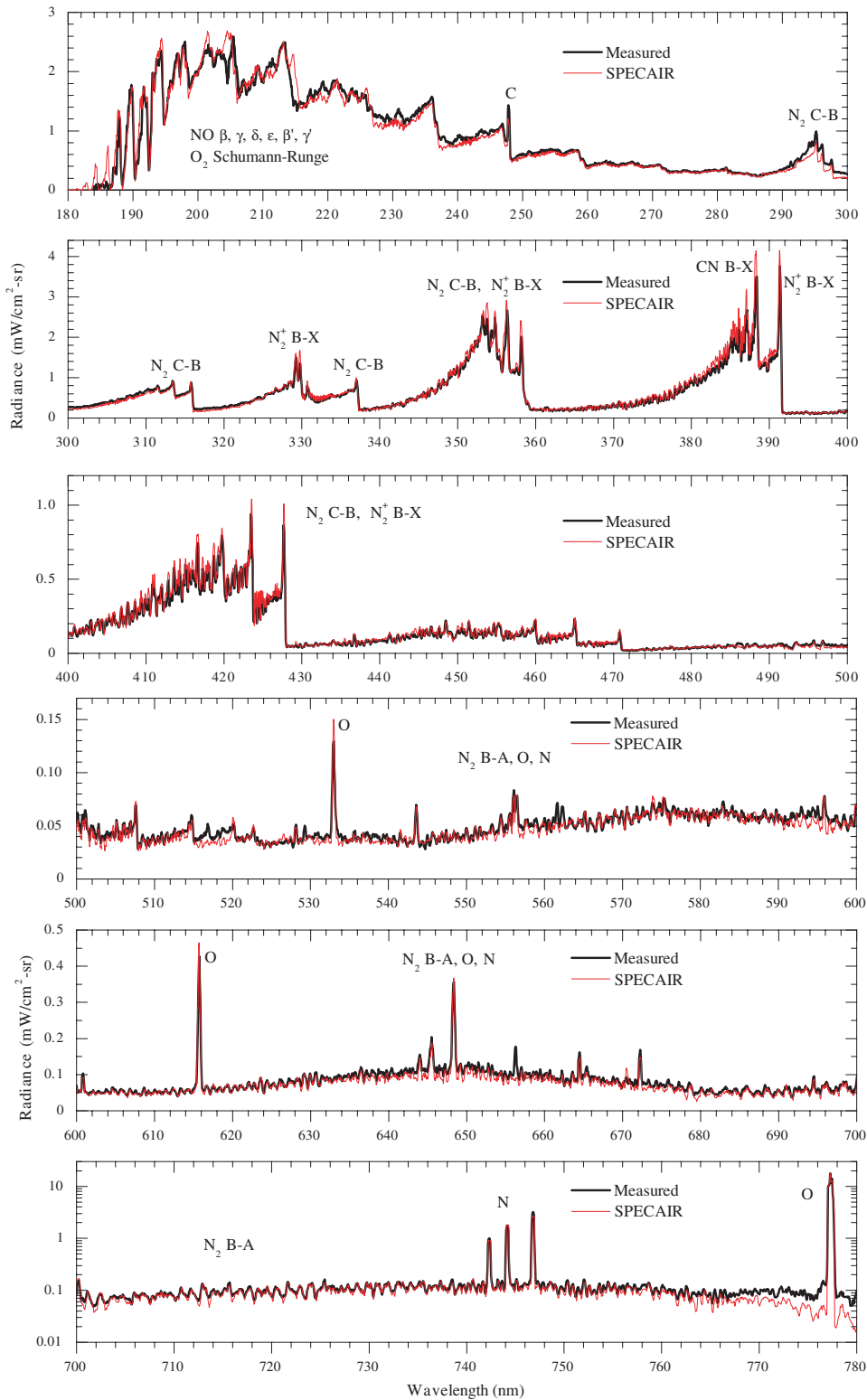
Figure 3. Comparison between SPECAIR and measured spectrum of LTE air at ∼7500 K.

result of preferential quenching of the rotational levels of OH [10]. To verify that the rotational levels follow a Boltzmann distribution, one should compare the measured spectrum to simulations assuming a Boltzmann distribution over the range 306–312 nm. If the rotational levels of the OH A state do not follow a Boltzmann distribution, it is not possible to directly infer the translational temperature of the gas from the OH A–X measurement.

3.1.3. Interferences. If platinum electrodes are used to produce the plasma by means of electrical discharge, one should be aware that the Pt I line at 306.47 nm may overlap

the peak of the *R* branch. In this case, narrower slit widths should be used to separate the Pt line from the OH spectrum.

We have used the OH transition to measure rotational temperatures in air/argon recombination experiments at gas temperatures below 4000 K [2], and also in glow experiments without discharge applied [3]. The OH spectrum measured in the glow experiments without discharge applied is shown in figure 9. The good agreement between simulated and predicted spectra over the entire range 306–312 nm proves that self-absorption is negligible and that the rotational levels follow a Boltzmann distribution.

3.2. NO A–X and N_2 C–B rotational temperature measurements

At higher temperatures or higher plasma excitation such as for the conditions of figure 1(*c*) with the electrical discharge applied, the OH emission spectrum becomes obscured by other emission syste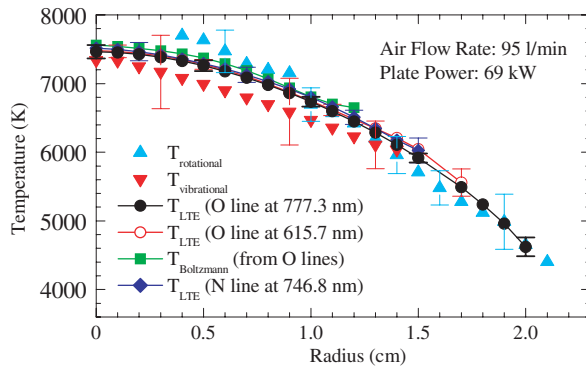ms. The rotational temperature can then be measured from the NO A–X (γ) or N_2 C–B (second positive system) transitions.

The NO γ technique proposed by Gomès *et al* [7] is based on the width of the (0, 1) band. Gomès *et al* [7] used the technique to measure rotational temperature of atmospheric pressure air plasmas in the range 3000–5000 K with a quoted accuracy of 250 K.

Spectroscopic measurements of the N_2 C–B transition are illustrated in figure 10, which shows a spectrum obtained in the glow discharge experiments of Yu *et al* [3]. The slit function is a trapezoid of base 0.66 nm and top 0.22 nm. The rotational temperature was determined by fitting the spectrum with SPECAIR in the range 260–382 nm. This spectral range corresponds the $\Delta v = -2$ vibrational band sequence of N_2 C–B. The best-fit SPECAIR spectrum yields a rotational temperature of 2200 ± 50 K, which is very close to the temperature measured from OH A–X without the discharge applied. The SPECAIR fit also yields a vibrational temperature of 3400 ± 50 K, based on the relative intensities of the (0, 2), (1, 3), (2, 4), and (3, 5) vibrational bands of the N_2 C state. It should be noted that the vibrational temperature of the C state is not necessarily the same as the vibrational temperature of the ground state of N_2.

Figure 11 shows the predicted spectral width of the (0, 2) band of N_2 C–B at 20% and 40% of the peak intensity, as a function of the rotational temperature. These simulations were made with SPECAIR, assuming a trapezoidal slit function of base 0.66 and top 0.22 nm. The width curves provide a quick way to estimate the rotational temperature if a full spectral model is not available.

3.3. N_2^+ B–X rotational temperature measurements

At higher excitation levels, the NO gamma and N_2 second positive systems suffer from increasing overlap by transitions

Figure 4. Measured electronic, vibrational and rotational temperature profiles in LTE air.
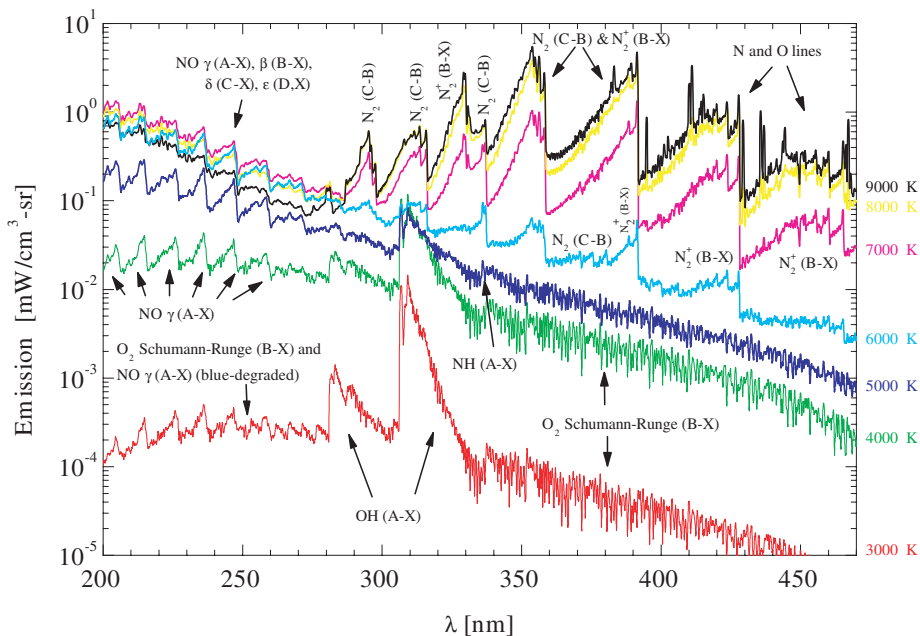

Figure 5. Ultraviolet emission spectra of LTE air at atmospheric pressure with 1.3% mole fraction of water vapour. These simulations were performed with SPECAIR, using a trapezoidal instrumental broadening function of base 0.66 nm and top 0.22 nm.
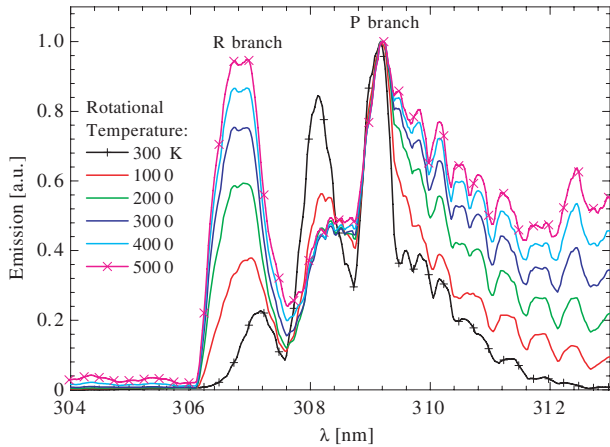
Figure 6. SPECAIR simulations of OH A–X (0, 0) emission normalized to *P*-branch peak, as a function of the rotational temperature.
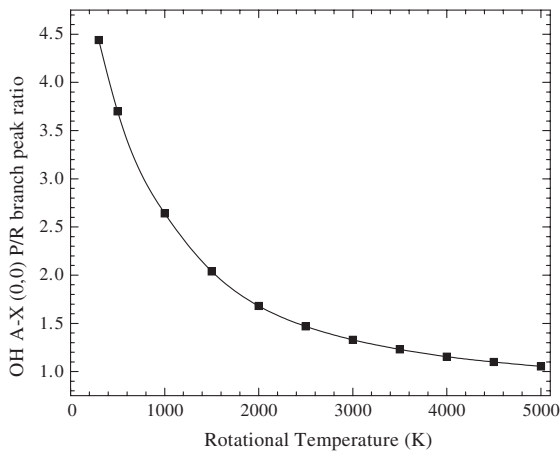

Figure 7. Ratio of the peak intensities of the OH (0, 0) *P* and *R* branches as a function of rotational temperature. These simulations were performed with SPECAIR, using a trapezoidal instrumental broadening function of base 0.66 nm and top 0.22 nm.
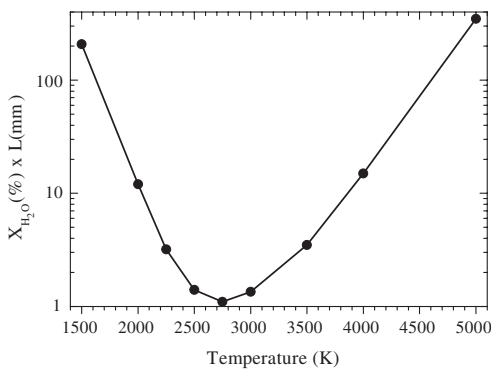

Figure 8. Optical thickness (in mm) times water vapour mole fraction (in %) resulting in 4% of self-absorption at peak of OH (0, 0) *P*-branch (309.2 nm) in atmospheric pressure equilibrium air.

from higher NO states (NO delta, epsilon), and by the O_2 Schumann–Runge, CN violet, and N_2^+ first negative band systems. The N_2^+ first negative system (B–X transition) can be used to measure the rotational temperature, provided that
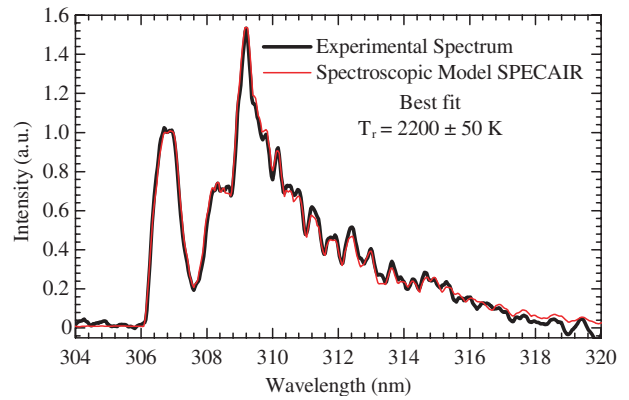

Figure 9. Experimental spectrum measured for the conditions of figure 1(*c*) with no electric field applied, and best-fit SPECAIR spectrum. The best-fit temperature is 2200 ± 50 K.
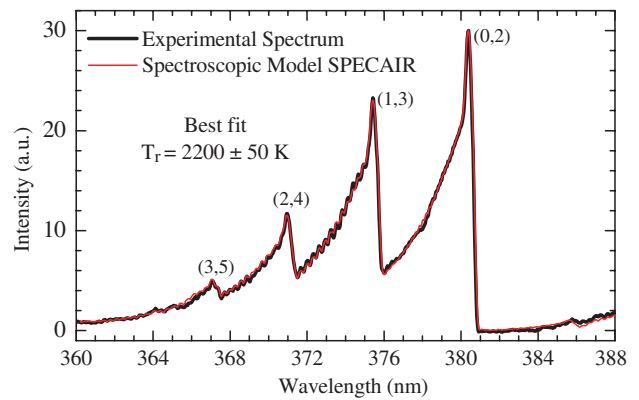

Figure 10. Measured N_2 C–B spectrum in the atmospheric pressure air glow discharge (conditions of figure 1(*c*)). SPECAIR best-fit provides a rotational temperature of 2200 ± 50 K.
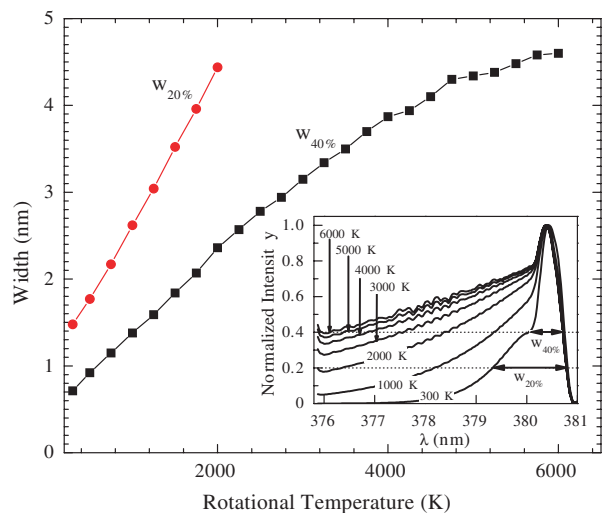

Figure 11. Spectral widths of the N_2 C–B (0, 2) band at 20% and 40% of the peak's height. These calculations were made with SPECAIR assuming a trapezoidal slit function of base 0.66 and top 0.22 nm. The inset shows the (0, 2) band spectra at various rotational temperatures, normalized to the intensity of the peak at 380.4 nm.

an accurate spectroscopic model is available to extract N_2^+ lines from the encroaching lines of CN and N_2 that emit in the same spectral range. The modelling is complicated by perturbations that affect the positions, intensities, and splitting of the N_2^+ lines. Recent spectroscopic analyses by Michaud *et al* [11] have provided accurate spectroscopic constants, incorporated in SPECAIR, that enable the precise identification of high rotational lines of N_2^+ B–X up to rotational quantum numbers of about 100. We showed in [8] that the group of rotational lines $R(70)$ and $P(97)$ at 375.95 nm are well isolated from lines of other transitions, and that the intensity of these two lines relative to the bandhead of the N_2^+ B–X $(0, 0)$ band at 391.55 nm is a very sensitive function of the rotational temperature. This technique was successfully applied to rotational temperature measurements in a nonequilibrium recombining nitrogen/argon plasma at the exit of a 15 cm test-section (figure 1(*b*)) [8]. The rotational temperature was measured to be 4850±100 K, an accuracy far superior to that of other N_2^+ rotational temperature measurement techniques (see for instance the review by Scott *et al* [12]).

4. Measurements of charged species concentrations

4.1. Electron number density

In plasmas with electron number densities greater than $\sim 5 \times 10^{13}$ cm^{-3}, spatially and temporally resolved electron number density measurements can be made from the lineshape of the Balmer β transition (4–2) of atomic hydrogen at 486.1 nm. This technique requires the addition to the plasma of a small amount (typically 1% or 2% mole fraction) of hydrogen, which may either come from dissociated water vapour in humid air or from premixing H_2 into the air stream. For detection by emission spectroscopy, the population of the $n = 4$ electronic state of atomic hydrogen must be high enough for the H_β line to be distinguishable from underlying air plasma emission (mostly due to the B–A or second positive system of N_2). This condition is usually fulfilled in equilibrium air plasmas with temperatures greater than 4000 K, or in nonequilibrium plasmas with sufficient excitation of hydrogen electronic states.

The lineshape of the H_β transition is determined by Lorentzian (Stark, van der Waals, resonance, natural) and Gaussian (Doppler, instrumental) broadening mechanisms that result in a Voigt profile. The Lorentzian half-width at half-maximum (HWHM) is the sum of the Lorentzian HWHMs. The Gaussian HWHM is the square root of the sum of the squared Gaussian HWHMs. If monochromator slits of equal width are used, the instrumental slit function is well approximated by a Gaussian profile. Numerical expressions for the Stark, van der Waals, resonance, Doppler, and natural HWHMs are derived below for the case of an air plasma with a small amount (a few per cent) of hydrogen.

4.1.1. Stark broadening.
Stark broadening results from Coulomb interactions between the radiator (here the hydrogen atom) and the charged particles present in the plasma. Both ions and electrons induce Stark broadening, but electrons are responsible for the major part because of their higher relative velocities. The lineshape can be approximated by a Lorentzian except at the linecentre where electrostatic interactions with ions cause a dip. Classical electrodynamics calculations of the H_β lineshape were made in the late 1960s and early 1970s that culminated in the publication of Stark broadening tables by the National Bureau of Standards [13]. In these studies, ion broadening was treated in the quasi-static approximation by averaging the effect of the electric field created by the ions over the statistical distribution of ions assumed to be stationary. Measurements of the H_β lineshape conducted shortly after the publication of the tables showed that the dip was much smaller than predicted and that its depth was a function of ion dynamics [14, 15]. Subsequent ion dynamics calculations [16, 17] confirmed the breakdown of the quasi-static theory near the centre of the H_β line and predicted a much smaller dip than Vidal *et al* [13]. The Stark FWHM of the H_β transition remained however in good agreement (within 25%) with the earlier predictions of Vidal *et al* [13]. The revised computations also confirmed that the Stark broadening width is mostly a function of the free electron concentration, and a weak function of the temperature. The Stark HWHM expression given in table 1 corresponds to a fit of the widths listed by Gigosos and Cardeñoso [17] for electron densities between 10^{14} and 4×10^{17} cm^{-3} and for reduced masses comprised between 0.9 and 1.0, which covers all perturbers present in the air plasma except hydrogen. (The Stark broadening of hydrogen by hydrogen ions is neglected here because we assume that the mole fraction of hydrogen is less than a few per cent.) The fit is within ±5% of the values of Gigosos and Cardeñoso for temperatures up to 10 000 K, ±13% up to 20 000 K, and ±20% up to 40 000 K. If better precision is needed, the actual values of Gigosos and Cardenos can be substituted for the present fit.

4.1.2. Resonance broadening.
Resonance broadening is caused by collisions between 'like' particles (e.g. two hydrogen atoms) where the perturber's initial state is connected by an allowed transition to the upper or lower state of the radiative transition under consideration. Typically, the three perturbing transitions that must be considered are g → l, g → u, and l → u, where g stands for the ground electronic state, and l and u for the lower and upper states of the radiative transition. Using the expression given by Griem ([18], p 97), we obtain

$$\Delta\lambda_{\text{resonance}} = \underbrace{\frac{3e^2}{16\pi^2\varepsilon_0 m_e c^2}}_{6.72\times 10^{-16}\,\text{m}^{-2}} \lambda_{\text{ul}}^2 \left[\lambda_{\text{lg}} f_{\text{gl}} \sqrt{\frac{g_g}{g_l}} n_g + \lambda_{\text{ug}} f_{\text{gu}} \sqrt{\frac{g_g}{g_u}} n_g \right.$$
$$\left. + \lambda_{\text{ul}} f_{\text{lu}} \sqrt{\frac{g_l}{g_u}} n_l \right], \qquad (1)$$

Table 1. HWHM (in nm) for the H_β line at 486.132 nm. P is the pressure in atm, T the gas temperature in K, n_e the electron number density in cm^{-3}, and X_H the mole fraction of hydrogen atoms.

$\Delta\lambda_{\text{Stark}}$	$\Delta\lambda_{\text{resonance}}$	$\Delta\lambda_{\text{van der Waals}}$	$\Delta\lambda_{\text{Natural}}$	$\Delta\lambda_{\text{Doppler}}$
$1.0 \times 10^{-11} (n_e)^{0.668}$	$30.2 X_H (P/T)$	$1.8 P/T^{0.7}$	3.1×10^{-5}	$1.74 \times 10^{-4} T^{0.5}$

Using the constants of Wiese *et al* [19] ($\lambda_{ul} = 486.132$ nm, $\lambda_{lg} = 121.567$ nm, $\lambda_{ug} = 97.2537$ nm, $g_u = 32$, $g_g = 2$, $g_l = 8$, $f_{gl} = 0.4162$, $f_{gu} = 0.02899$, $f_{lu} = 0.1193$), we obtain the resonance HWHM listed in table 1.

4.1.3. Van der Waals broadening. Van der Waals broadening is caused by collisions with neutral perturbers that do not share a resonant transition with the radiating particle. Griem ([18], p 99) gives the following expression for radiator r colliding with perturber p:

$$\Delta\lambda_{\text{van der Waals}} \approx \frac{\lambda_{ul}^2}{2c} \left(\frac{9\pi\hbar^5 \overline{R_\alpha^2}}{16m_e^3 E_p^2} \right)^{2/5} \overline{v_{rp}^{3/5}} N_p, \qquad (2)$$

where v_{rp} is the relative speed of the radiating atom and the perturber, E_p is the energy of the first excited state of the perturber connected with its ground state by an allowed transition, N_p is the number density of the perturber, and the matrix element $\overline{R_\alpha^2}$ is equal to:

$$\overline{R_\alpha^2} \approx \frac{1}{2} \frac{E_H}{E_\infty - E_\alpha} \left[5 \frac{z^2 E_H}{E_\infty - E_\alpha} + 1 - 3l_\alpha(l_\alpha + 1) \right]. \qquad (3)$$

In equation (3), E_H and E_∞ are the ionization energies of the hydrogen atom and of the radiating atom, respectively, E_α is the term energy of the upper state of the line, l_α its orbital quantum number, and z is the number of effective charges ($z = 1$ for a neutral emitter, $z = 2$ for a singly ionized emitter, etc). For H_β, we have $E_H = E_\infty = 13.6$ eV, $E_\alpha = 12.75$ eV, and $z = 1$. The H_β transition is a multiplet of 7 lines (see table 3) originating from upper states 4s, 4p, and 4d of orbital angular momenta $l_\alpha = 0$, 1, and 2. For $l_\alpha = 0$, 1, and 2, $(\overline{R_\alpha^2})^{2/5}$ takes the values 13.3, 12.9, and 12.0, respectively. As listed in table 3, the components issued from the 4s, 4p, and 4d states represent 1.9%, 21.6%, and 76.5% of the total H_β emission, respectively. We use these percentages as weighting factors to determine an average value of $(\overline{R_\alpha^2})^{2/5} = 12.2$.

We find that the relative velocity term $\overline{v_{rp}^{3/5}}$ of equation (2) can be related to the mean speed as follows:

$$\overline{v_{rp}^{3/5}} = \left(\frac{4}{\pi} \right)^{2/10} \Gamma\left(\frac{9}{5} \right) (\bar{v}_{rp})^{3/5} \cong 0.98(\bar{v}_{rp})^{3/5}$$

$$= 0.98 \left(\frac{8kT}{\pi m_{rp}^*} \right)^{3/10} \qquad (4)$$

where m_{rp}^* is the reduced mass of the radiator–perturber pair.

Summing over all perturbers present in the plasma, and introducing the mole fraction X_p of perturber p,

equation (2) becomes

$$\Delta\lambda_{\text{van der Waals}} \approx 0.98 \frac{\lambda_{ul}^2}{2c} \left(\frac{9\pi\hbar^5 \overline{R_\alpha^2}}{16m_e^3 E_p^2} \right)^{2/5} \left(\frac{8kT}{\pi} \right)^{3/10}$$

$$\times \frac{P}{kT} \sum_p \left[\frac{X_p}{E_p^{4/5} (m_{rp}^*)^{3/10}} \right], \qquad (5)$$

In air plasmas, O, N, N_2, O_2, and NO represent 98% of the chemical equilibrium composition for temperatures up to 10 000 K. We computed the equilibrium mole fractions of these 5 species up to 10 000 K and combined them with the E_p's and m_{rp}^*'s listed in table 2 in order to evaluate the summation term in equation (5). The value of this term is found to be approximately constant over the entire temperature range and equal to 0.151 ($\pm$0.007). The final expression for the van der Waals HWHM of H_β in air plasmas with a small amount of hydrogen added is given in table 1.

4.1.4. Doppler broadening. If a particle approaching an observer with a relative speed v emits a photon of frequency ν_0 (or wavelength λ_0) in the reference frame of the particle, the wavelength λ of the photon detected by the observer appears shifted from λ_0 as a consequence of the Doppler effect. For a collection of emitters with a Maxwellian velocity distribution (characterized by a temperature T_h), the lineshape of the transition is a Gaussian function, with a Doppler HWHM of ([18], p 101):

$$\Delta\lambda_{\text{Doppler}} = \frac{1}{2}\lambda_{ul}\sqrt{\frac{8kT_h \ln 2}{m_h c^2}}$$

$$= 3.58 \times 10^{-7}\lambda_{ul}\sqrt{\frac{T_h \text{ [K]}}{\hat{M}_h \text{ [g mol}^{-1}]}}. \qquad (6)$$

The Doppler HWHM of H_β is given in table 1.

4.1.5. Natural broadening. Natural broadening is a consequence of the Heisenberg uncertainty principle applied to the energies of the initial and the final states of the transition. The uncertainty on the transition frequency or wavelength translates into a Lorentzian line profile of HWHM:

$$\Delta\lambda_{\text{Natural}} = \frac{\lambda_{ul}^2}{4\pi c} \left(\sum_{n<u} A_{un} + \sum_{n<l} A_{ln} \right), \qquad (7)$$

In equation (7), the two summation terms represent the inverses of the transition's upper and lower level lifetimes. They can be calculated using the Einstein A coefficients of Wiese *et al* [19]. As can be seen from table 1, natural broadening is negligible in comparison with the other mechanisms.

Table 2. Constants needed in equation (5) when the radiator is a hydrogen atom.

Perturber	M_{rp}^* (g mole^{-1})	Transition issued from the first excited state optically connected to the ground state	E_p (eV)	$M_{rp}^{*-0.3} E_p^{-0.8}$ (g mol^{-1})$^{-0.3}$eV$^{-0.8}$
O	0.94	$^3S^0 \to {}^3P$	9.5	0.17
N	0.93	$^4P \to {}^4S^0$	10.3	0.16
O_2	0.97	B $^3\Sigma_u^- \to$ X $^3\Sigma_g^-$ (Schumann–Runge)	6.2	0.23
N_2	0.97	b $^1\Pi_u \to$ X $^1\Sigma_g^+$ (Birge–Hopfield 1)	12.6	0.13
NO	0.97	A $^2\Sigma^+ \to$ X $^2\Pi$ (gamma)	5.5	0.26

Table 3. Components of the H_β transition multiplet and their properties.

Wavelength air (nm)	A_{ul} (s^{-1})	Upper level configuration	Lower level configuration	g_u	g_l	Relative intensity (% of total H_β emission)
486.127 85	1.718×10^7	4d ^{2}D$_{3/2}$	2p ^{2}P$^0_{1/2}$	4	2	25.5
486.128 69	9.668×10^6	4p ^{2}P$^0_{3/2}$	2s ^{2}S$_{1/2}$	4	2	14.4
486.128 83	8.593×10^5	4s ^{2}S$_{1/2}$	2p ^{2}P$^0_{1/2}$	2	2	0.6
486.129 77	9.668×10^6	4p ^{2}P$^0_{1/2}$	2s ^{2}S$_{1/2}$	2	2	7.2
486.136 14	2.062×10^7	4d ^{2}D$_{5/2}$	2p ^{2}P$^0_{3/2}$	6	4	45.9
486.136 50	3.437×10^6	4d ^{2}D$_{3/2}$	2p ^{2}P$^0_{3/2}$	4	4	5.1
486.137 48	1.719×10^6	4s ^{2}S$_{1/2}$	2p ^{2}P$^0_{3/2}$	2	4	1.3

4.1.6. Fine structure effects. Because of fine structure spin–orbit splitting in the upper and lower levels, the H_β transition is in fact a multiplet of seven lines (see table 3). The resulting lineshape is the sum of these lines, each of which can be calculated with the broadening widths listed in table 1. The resulting lineshape will be close to a Voigt profile only if the HWHM of each line is much greater than 0.005 nm, half the separation between the extreme lines. The technique presented below should only be used when the measured HWHM is much greater than 0.005 nm. As will be seen below, this condition is fulfilled in most situations of practical interest.

4.1.7. Electron density measurements in equilibrium air plasmas. We have employed this technique to measure electron number densities in air and nitrogen plasmas under various degrees of nonequilibrium [1, 2]. We first describe measurements made in the LTE air plasma corresponding to the conditions of figure 1(a) and the temperature profile of figure 4. We used a $\frac{3}{4}$-m monochromator with a 1200-groove mm^{-1} grating, and entrance and exit slits of 20 μm. The instrumental slit function was approximately Gaussian with HWHM of 0.011 nm. A small amount of H_2 (1.7% mole fraction) was premixed with air before injection into the plasma torch. The spatial resolution of the measurements, determined by the width of the entrance slit and the magnification of the optical train, was approximately 0.13 mm.

Figure 12 shows the line-of-sight emission spectrum measured along the plasma diameter. Also shown in figure 12 is the 'background' emission spectrum, which is mainly due to the N_2 B $^3\Pi_g$–A $^3\Sigma_u^+$ first positive system. This background was measured after switching off the hydrogen flow. Without hydrogen, we measured the plasma temperature to be lower by approximately 200 K. The torch power was slightly readjusted in order to return to the same temperature conditions by matching the intensity of the background spectral features away from the H_β linecentre. Figure 13 shows the H_β lineshape obtained by subtracting the background signal from the total spectrum. The measured lineshape is well fitted with a Voigt profile of HWHM = 0.11 nm. For these conditions, the HWHMs of the various broadening mechanisms and of the resulting Voigt profile are shown in figure 14. The measured HWHM corresponds to an electron number density of approximately 1.0×10^{15} cm^{-3}. Because the intensity of the H_β line is proportional to the population of hydrogen in excited state $n = 4$, which is a strong function of the temperature ($n_4 \sim \exp[-150\,000/T]$), the line-of-sight-integrated emission scan is dominated by emission from the hot central plasma core. Therefore, the line-of-sight measurement
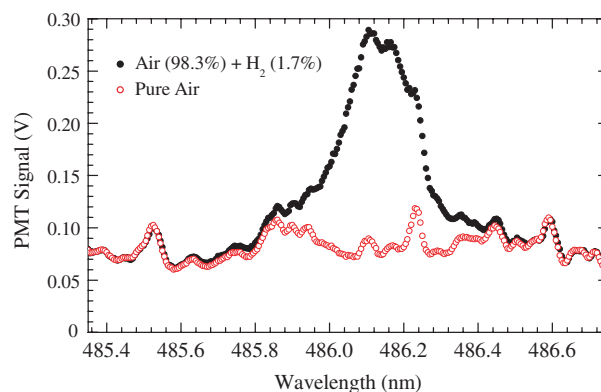

Figure 12. Typical emission scan of the H_β line. The underlying emission features are mostly from the first positive system of N_2.
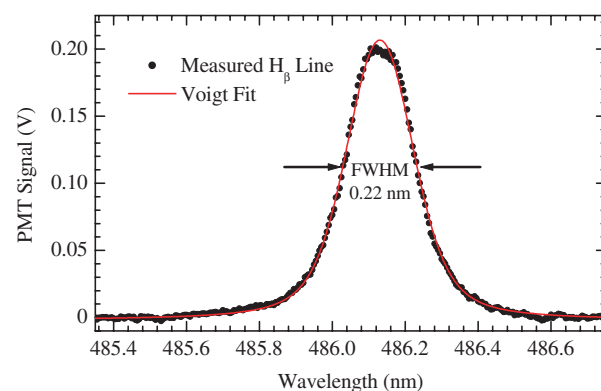

Figure 13. H_β lineshape obtained from the difference of the two signals shown in figure 12, and Voigt fit.

provides, to good approximation, the electron density at the centreline of the plasma.

We also measured the radial profile of electron number density. To this end, we scanned the H_β lineshape at 25 lateral locations along chords of the 5-cm diameter plasma, and we obtained the lineshapes at each radial location using an Abel-inversion. Figure 15 shows the radial electron density profile determined from the Abel-inverted lineshapes. Figure 15 also shows the radial profile of chemical equilibrium electron densities based on the measured LTE temperature of the oxygen line at 777.3 nm. The good agreement between the two profiles provides validation of the technique. Note that the electron density of 1.0×10^{15} cm^{-3} determined from the line-of-sight integrated lineshape is consistent with the Abel-inverted electron densities in the central core of the plasma.
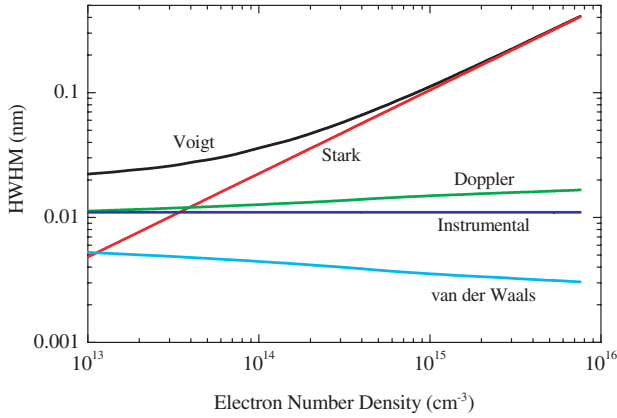
Figure 14. H$_\beta$ lineshape broadening as a function of the electron number density in LTE air at atmospheric pressure. (Instrumental HWHM = 0.011 nm.) The resonance broadening HWHM is less than 2×10^{-4} nm for the conditions of this graph.

Figure 15. Measured (——) and equilibrium (- - - -) electron number density profiles.

Figure 16. H$_\beta$ lineshape in a low temperature ($\sim$4500 K) LTE air plasma. Here, the H$_\beta$ lineshape was measured in second order to reduce the instrumental broadening width by a factor of 2 relative to other broadening widths.

Figure 16 shows another example of H$_\beta$ lineshape measurement in an LTE air plasma with a temperature peaked at about 4500 K. Instrumental broadening in this case (HWHM = 0.015 nm) was not negligible relative to Stark broadening. To improve the sensitivity we measured the spectrum in the second order of the grating. This had the
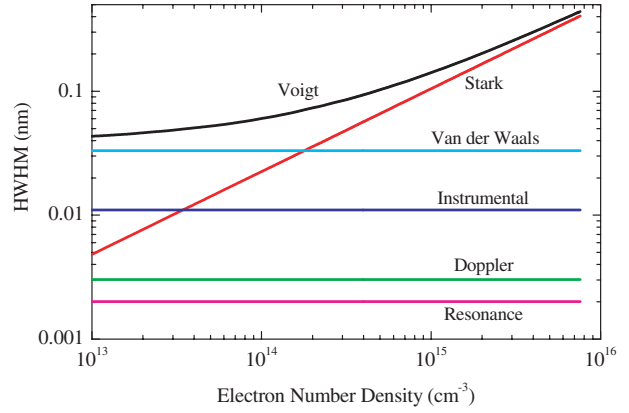
Figure 17. H$_\beta$ lineshape broadening as a function of the electron number density in nonequilibrium atmospheric pressure air at a gas temperature of 300 K. (Instrumental HWHM = 0.011 nm.)
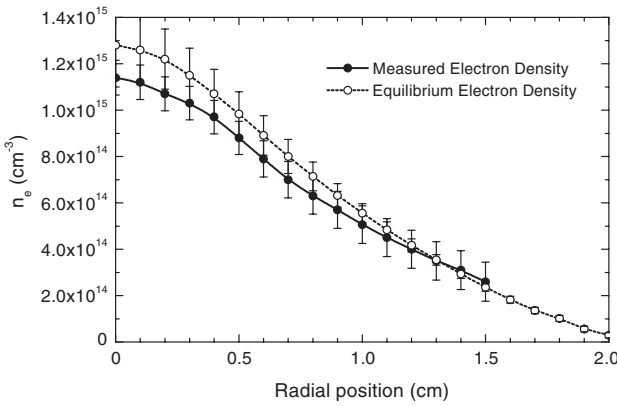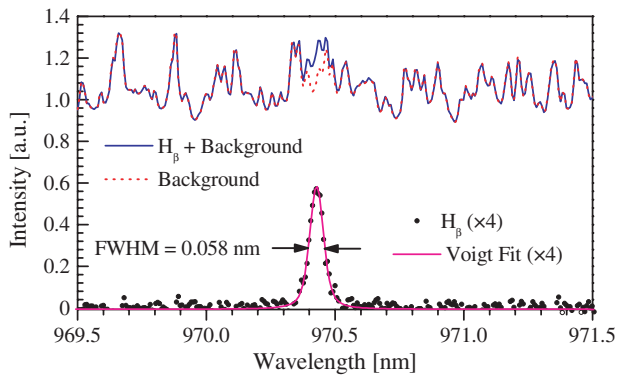
effect of reducing instrumental broadening by a factor of 2 with respect to the other broadening widths. CCD averaging times of 10 s were employed. The inferred electron number density of 5×10^{13} cm^{-3} represents a lower detection limit in equilibrium air plasmas because the intensity of the H$_\beta$ line becomes very weak relative to the underlying N$_2$ first positive signal.

4.1.8. Electron density measurements in nonequilibrium air plasmas. Of the broadening mechanisms plotted in figure 14, only the Stark broadening depends explicitly on the electron density. The Doppler, van der Waals and resonance broadening widths depend on the gas temperature. For LTE plasmas the electron number density is a unique function of the temperature and pressure, as given by the Saha equation. In figure 14, we have made use of the Saha equilibrium relation to plot all broadening widths as a function of the equilibrium electron number density. In this regard, the Voigt widths shown in figure 14 should be used to determine the electron number density only in equilibrium air plasmas. In nonequilibrium plasmas, the Doppler, van der Waals, and resonance widths should be replaced with values based on the actual gas temperature. Figure 17 illustrates this case for a nonequilibrium plasma with a gas temperature of 300 K. The limiting sensitivity factor at low temperature is the van der Waals broadening, which becomes effectively larger than Stark broadening at electron densities smaller than 2×10^{14} cm^{-3}. It is therefore essential, as done in figure 17, to correct the measurements for van der Waals broadening in low temperature plasmas. An example of application of this technique to nonequilibrium air and nitrogen plasmas may be found in [2].

4.2. Cavity ring-down spectroscopy

As discussed in the previous section, the electron density can be determined from H$_\beta$ Stark-broadened lineshapes down to densities of about 5×10^{13} cm^{-3} in atmospheric pressure air plasmas. Below this value, the electron density can be determined by measuring the concentration of the dominant positive ion. A sensitive technique is required because ions are trace species in weakly ionized plasmas.

Cavity ring-down spectroscopy (CRDS) is a sensitive direct-absorption technique that has been successfully employed in our laboratory to detect dilute concentrations of N_2^+ in atmospheric pressure air and nitrogen plasmas [20–22]. N_2^+ tends to the dominant ion in nitrogen plasmas at temperatures below ~ 6000 K, and under these conditions the N_2^+ measurement enables one of the most direct measurements of electron number density. In LTE air, the concentration of N_2^+ may be linked to that of electrons through chemical equilibrium relations. In nonequilibrium plasmas, a collisional-radiative model may be used to relate the ion and electron concentrations [21].

In CRDS, light from a pulsed or continuous-wave laser source is injected into a high-finesse optical cavity (the ring-down cavity) formed by two or more highly reflective mirrors [23, 24]. With the input radiation terminated, light trapped in the ring-down cavity, I_{circ}, decays exponentially [25] with time, t:

$$I_{circ}(t) = I_{circ}(t_0) \exp\left[-\frac{(\alpha[c]l_{rt} + n(1-R) + L) \times (t-t_0)}{T_{rt}}\right],$$

where T_{rt} is the round-trip transit time, R is the mirror reflectivity, α is the absorption cross-section of the absorbing species present within the cavity at concentration $[c]$, n is the number of mirrors that comprise the cavity, l_{rt} is the round-trip pathlength of the cavity, and L accounts for other losses within the cavity including absorption and scattering by the mirror surfaces. By fitting the ring-down waveform to the function $I_0 \exp[-t/\tau]$, the decay rate, $1/\tau$, may be determined. This decay or 'ring-down' rate is simply related to the concentration of absorbing species within the ring-down cavity:

$$\frac{1}{\tau} = \frac{\alpha[c]l_{rt} + n(1-R) + L}{T_{rt}}.$$

By plotting the decay rate as a function of wavelength, an absorption spectrum of species present within the cavity is generated. If the empty-cavity decay rate, $1/\tau_0$, and absorption cross section of the absorbing species are known, then the absolute concentration of absorbing species is determined from:

$$[c] = \left(\frac{1}{\tau} - \frac{1}{\tau_0}\right) \times \left(\frac{T_{rt}}{\alpha l_{rt}}\right).$$

4.2.1. Cavity ring-down measurements of N_2^+ in an LTE air plasma. Figure 18 shows the schematic of our CRDS experiments with an atmospheric pressure LTE air plasma. A tunable Nd : YAG pumped dye laser and a two-mirror ring-down cavity are used to probe the rotationally resolved N_2^+ B–X (0, 0) absorption spectrum from 387.0 to 392.0 nm. Pulses of light from the laser system (8–12 mJ per pulse, 8 ns duration) are mode-matched to the ring-down cavity using a pair of lenses (5.0-cm focal length) and a pinhole (0.25 mm diameter). The ring-down cavity, 2.1 m in length, is comprised of two high reflectivity mirrors (Los Gatos Research, $R = 0.9993$, radius-of-curvature: 6 m) mounted to an aluminium rail 3 m in length. The rail may be translated, allowing the ring-down cavity axis to sample different portions of the air plasma. By carefully aligning the beam parallel to the translation axis of the rail, the ring-down cavity may be translated across the plasma orifice (7 cm in diameter) while maintaining alignment
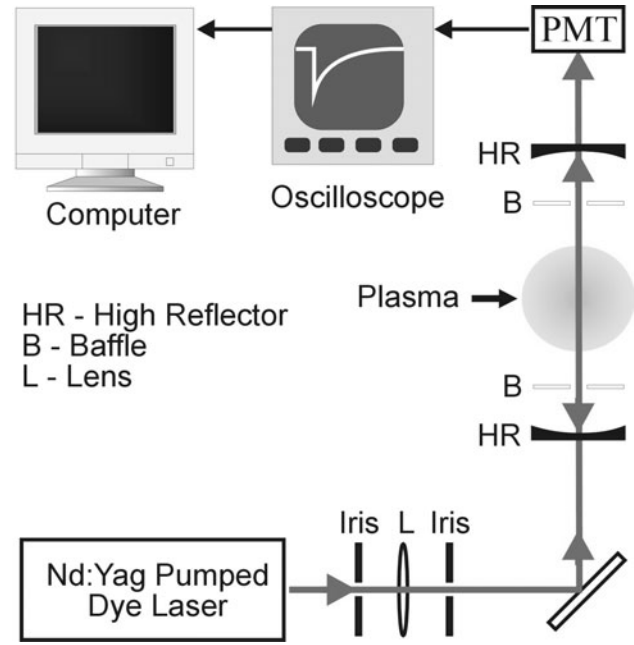

Figure 18. Schematic diagram of CRDS set-up used to probe N_2^+.

between the laser and the ring-down cavity. By translating the cavity relative to the plasma, we obtain ring-down spectra at lateral locations. These spectra are Abel-inverted to provide radial profiles. Baffles (6 mm aperture) are mounted in the ring-down cavity to reduce the background light intensity at the detector and to protect the cavity mirrors from the large amount of ultraviolet radiation generated by the air plasma. A mirror mounted to the translating rail deflects the light exiting the cavity onto a fast photomultiplier tube (Hamamatsu PMT R1104) located several metres from the ring-down cavity. Current generated by the photomultiplier is digitized using a digitizing oscilloscope, and a computer is then used to fit the decay waveforms to an exponential function and extract $1/\tau$, while scanning the laser through the wavelength range of interest. Emission spectroscopy was performed in parallel with the CRDS measurements to provide an independent plasma temperature profile from Abel-inverted measurements of the absolute intensity of the 777.3 nm oxygen line.

With the RF plasma torch off, the empty cavity decay lifetime, τ_0, was typically 10 μs. With the RF plasma on, however, τ_0 decreased to 0.65 μs, even with the cavity translated 2.5 cm beyond the edge of the plasma torch orifice. This decrease in τ was attributed to two loss mechanisms within the cavity. The first was linked to the existence of a long-lived gas-phase species generated by the plasma torch, possibly O_3 or NO_2, which possesses a broad featureless absorption transition in the wavelength of interest. The concentration of this background absorber fluctuates in the turbulent air surrounding the plasma causing shot-to-shot fluctuations in τ. These fluctuations decrease the sensitivity of the absorption measurement and increase in severity as the cavity is translated toward the edge of the plasma where the laser beam samples more of the surrounding air. We obtained some reduction in this background absorption by purging the turbulent region surrounding the plasma with dry nitrogen. The second source of noise is caused by irradiation of the dielectric mirrors by UV

radiation from the air plasma. UV-induced reduction in the reflectivity of dielectric mirrors has been observed previously [26] and was attributed to deformation of the top dielectric layer after absorption of UV photons with energies of a few electronvolt. The effect of UV radiation on the reflectivity of the dielectric mirrors used in this work was examined by translating the ring-down cavity well outside the air plasma and shielding the mirrors from plasma radiation. A 50% increase in τ was observed when the mirrors were shielded from plasma radiation. Rapid recovery of mirror reflectivity was observed when the RF torch was extinguished. Therefore, fluctuations in the intensity of UV radiation from the RF torch produce fluctuations in the observed cavity decay lifetime τ. Finally, we note that thermal lensing of the laser beam by the plasma has not been identified as a major source of loss within the ring-down cavity.

The linewidth of the laser, estimated to be $0.5\,\mathrm{cm}^{-1}$ from fitted linewidths, determined the spectral resolution of the CRDS technique. The free spectral range of the high-finesse ring-down cavity was approximately 71 MHz, roughly 200 times smaller than the linewidth of the laser. This condition ensured the coupling of light into the ring-down cavity because many longitudinal modes of the cavity were excited during the laser pulse. By filtering the laser output with a pinhole and through careful alignment of the ring-down cavity, excitation of transverse modes within the ring-down cavity was minimized. Interference between transverse modes at the detector is typically the dominant noise source in pulsed-laser ring-down experiments [27]. Final alignment of the cavity was complete when the amplitude of these oscillations was reduced to less than 10% of the initial amplitude of the ring-down waveform.

Figure 19 shows the absorbance spectrum of N_2^+ near the B–X $(0, 0)$ bandhead measured with the CRDS technique, as well as the effective absorbance spectrum predicted by SPECAIR. By 'effective', we mean that the calculated absorbance spectrum is convolved with the laser lineshape, estimated to be Gaussian of FWHM $= 0.5\,\mathrm{cm}^{-1}$. Each spectral element represents an average of 10 decay rates, each obtained by fitting a waveform that was itself an average of 25 single-shot waveforms. As pointed out by Zalicki and Zare [24], the CRDS signal is well approximated by a single exponential only when the ratio κ of sample absorbance per pass to the cavity loss per pass is much less than unity. In the present experiments, the peak sample absorbance per pass is approximately 0.0027 (figure 19) and the cavity loss per pass is given by

$$1 - R_{\mathrm{eff}} = \frac{l}{c\tau_0},$$

where $l = 2.1\,\mathrm{m}$ is the length of the cavity, c is the speed of light, and τ_0 is the cavity decay time away from lines of N_2^+. From the measured $\tau_0 = 0.65\,\mu\mathrm{s}$ we infer the cavity loss to be 0.011. Thus, $\kappa \cong 0.25$ and therefore we may expect non-exponential ring-down decays. The error incurred by fitting the decay with a single exponential can be quantified from the analysis presented by Yalin and Zare [28]. Figure 2 of [28] shows the ratio of apparent absorbance to actual absorbance as a function of the two reduced parameters κ and Δ, where Δ is the ratio of the FWHM of the laser (15 GHz here) to the FWHM of the absorption feature (10 GHz at most for the present experiment). It follows that, for our conditions ($\kappa \cong 0.25$, $\Delta \cong 1.5$), the experimental procedure underestimates the N_2^+ bandhead intensity by about 7%. After a few iterations (i.e. increase the apparent absorbance by 7% and repeat the foregoing analysis), we find that the actual peak absorbance is about 8% larger than measured. We conclude that the error resulting from non-exponential decays is less than 8%.

To determine the spatial profile of N_2^+ concentration, we measured the absorption by N_2^+ at 391.6 nm as the ring-down cavity was translated from the centre to the edge of the plasma at 0.2-mm intervals with a spatial resolution of 0.5 mm. We then employed an Abel transform to extract N_2^+ absorption as a function of radial distance from the centre of the plasma. Separately, using SPECAIR we calculated the spectral absorbance of N_2^+ as a function of the temperature, taking into account Doppler and pressure broadenings. We convolved the resulting spectra with the laser lineshape to obtain the effective spectral absorbance as a function of temperature. By comparing the actual measured absorbance and the predicted effective absorbance, we deduced the temperature of the plasma at each radial location. The radial concentration profile of N_2^+ (figure 20) was determined from chemical equilibrium relations since the plasma is in LTE.

The temperature profile of the air plasma, determined independently via emission spectroscopy, has a shape similar
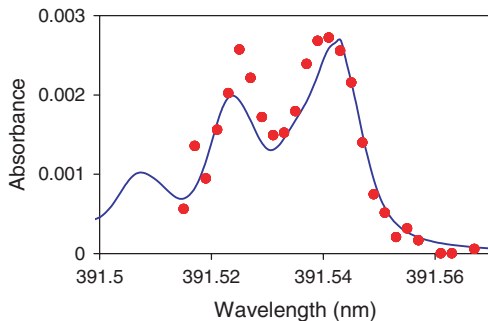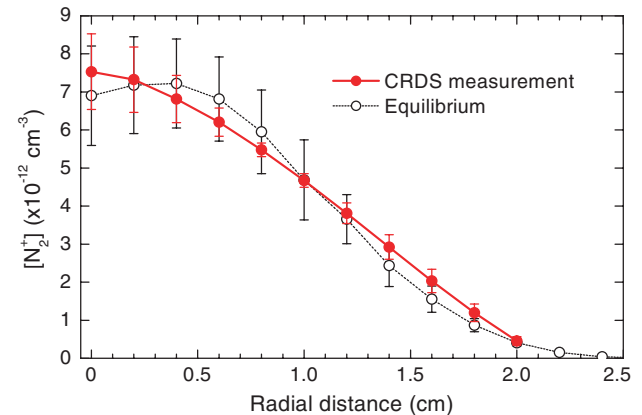

Figure 19. Experimental (●) and simulated (——) absorption spectrum of the N_2^+ B–X $(0, 0)$ bandhead in LTE air plasma with temperature profile peaked at 6500 K.

Figure 20. Concentration profiles of N_2^+ obtained by: (*a*) Abel-inversion of CRDS absorbance profile and (*b*) LTE calculation based on temperature profile obtained from Abel inverted absolute intensity profile of the 777.3 nm oxygen line.
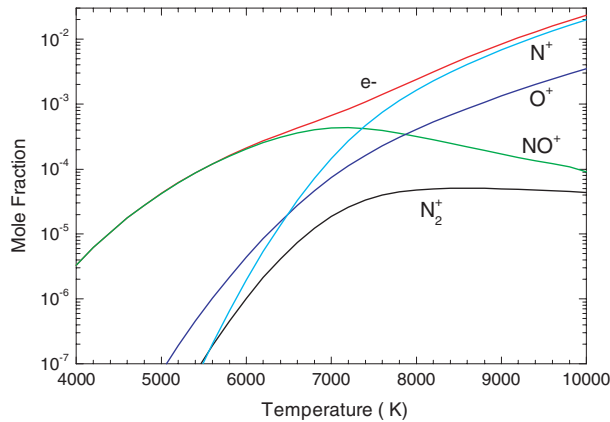
Figure 21. Mole fractions of the dominant charged species in LTE air at atmospheric pressure.

to that of figure 4 but is uniformly lower by about 1000 K. The LTE concentration profile of N_2^+ based on the measured LTE temperature profile is in excellent agreement with the CRDS measurements.

At these conditions, N_2^+ is not the dominant ion, and therefore is not equal to the electron density. Nevertheless, the electron density can be inferred from chemical equilibrium relations (see figure 21).

4.2.2. Cavity ring-down measurements of N_2^+ in a nonequilibrium nitrogen plasma. We have recently extended the CRDS technique to the measurement of N_2^+ in dc and pulsed nonequilibrium nitrogen glow discharges [21, 22]. In these experiments, we have demonstrated measurement of N_2^+ concentrations as low as approximately 7×10^{10} cm^{-3} with sub-millimetre spatial resolution and microsecond temporal resolution. For the conditions of these experiments (electron temperature close to 10 000 K), N_2^+ is the dominant ion and the measured N_2^+ concentration profiles are essentially identical to the electron number density profiles.

5. Conclusions

Several optical techniques have been presented for making measurements of temperature and charged species concentrations in air and nitrogen plasmas. These techniques can be applied to both equilibrium and nonequilibrium air or nitrogen plasmas over a wide range of conditions, with sub-millimetre spatial resolution and sub-microsecond temporal resolution. The gas temperature is typically measured using medium-resolution emission spectroscopy of the rotational line structure of selected OH, NO, N$_2$, and N$_2^+$ vibrational bands. The limitations and potential difficulties associated with these techniques have been discussed. Electron densities above approximately 5×10^{13} cm^{-3} can be measured from the Stark-broadened H$_\beta$ lineshape with appropriate corrections for other broadening mechanisms. The concentrations of ions, in particular N$_2^+$, can be measured by CRDS down to very low concentrations of about 7×10^{10} cm^{-3}. Through the use of charge neutrality and, for multiple ions, knowledge of ion chemistry, the concentration of N$_2^+$ ions can be related to the concentration of electrons. The CRDS technique thus provides

a way to measure electron densities beyond the range of sensitivity of the H$_\beta$ Stark broadening technique.

References

[1] Laux C O 1993 Optical diagnostics and radiative emission of air plasmas *PhD Thesis* Mechanical Engineering, Stanford University, Stanford, CA

[2] Gessman R J, Laux C O and Kruger C H 1997 Experimental study of kinetic mechanisms of recombining atmospheric pressure air plasmas *AIAA 97-2364, 28th AIAA Plasmadynamics and Lasers Conf. (Atlanta, GA)*

[3] Yu L, Packan D M, Laux C O and Kruger C H 2002 Direct-current glow discharges in atmospheric pressure air plasmas *J. Appl. Phys.* **91** 2678–86

[4] Yu L, Pierrot L, Laux C O and Kruger C H 2001 Effects of vibrational nonequilibrium on the chemistry of two-temperature nitrogen plasmas *Plasma Chem. Plasma Process.* **21** 483–503

[5] Laux C O, Gessman R J and Kruger C H 2002 Measurements and modeling of the absolute spectral emission of air plasmas between 185 and 800 nm in preparation
Laux C O 2002 Radiation and nonequilibrium collisional-radiative models (von Karman Institute Special Course on Physico-chemical Modeling of High Enthalpy and Plasma Flows, Rhode-Saint-Genèse, Belgium 4–7 June 2002)

[6] Park C 1985 *Nonequilibrium Air Radiation (NEQAIR) Program: User's Manual* (Moffett Field, CA: NASA-Ames Research Center) Technical Memorandum TM86707

[7] Gomès A M, Bacri J, Sarrette J P and Salon J 1992 Measurement of heavy particle temperature in a RF air discharge at atmospheric pressure from the numerical simulation of the NOγ system *J. Anal. At. Spectrosc.* **7** 1103–9

[8] Laux C O, Gessman R J, Kruger C H, Roux F, Michaud F and Davis S P 2001 Rotational temperature measurements in air and nitrogen plasmas using the first negative system of N$_2^+$ *J. Quant. Spectrosc. Radiat. Transfer* **68** 473–82

[9] Levin D A, Laux C O and Kruger C H 1999 A general model for the spectral radiation calculation of OH in the ultraviolet *J. Quant. Spectrosc. Radiat. Transfer* **61** 377–92

[10] Copeland R A and Crosley D R 1984 Rotational level dependence of electronic quenching of hydroxyl OH (A $^2\Sigma^+$, $v' = 0$) *Chem. Phys. Lett.* **107** 295–300

[11] Michaud F, Roux F, Davis S P, Nguyen A-D and Laux C O 2000 High resolution Fourier spectrometry of the ^{14}N$_2^+$ ion *J. Mol. Spectrosc.* **203** 1–8

[12] Scott C D, Blackwell H E, Arepalli S and Akundi M A 1998 Techniques for estimating rotational and vibrational temperatures in nitrogen arcjet flow *J. Thermophys. Heat Transfer* **12** 457–64

[13] Vidal C R, Cooper J and Smith E W 1973 Hydrogen Stark-broadening tables *Astrophys. J. Suppl. Ser.* **25** 37–136

[14] Kelleher D E and Wiese W L 1973 Observation of ion motion in hydrogen Stark profiles *Phys. Rev. Lett.* **31** 1431–4

[15] Wiese W L, Kelleher D E and Helbig V 1975 Variations in Balmer-line Stark profiles with atom-ion reduced mass *Phys. Rev.* A **11** 1854–64

[16] Kelleher D E, Wiese W L, Helbig V, Greene R L and Oza D H 1993 Advances in plasma broadening of atomic hydrogen *Phys. Scr.* T **47** 75-9

[17] Gigosos M A and Cardeñoso V 1996 New plasma diagnosis tables of hydrogen Stark broadening including ion dynamics *J. Phys. B: At. Mol. Opt. Phys.* **29** 4795–838

[18] Griem H R 1964 *Plasma Spectroscopy* (New York: McGraw-Hill)

[19] Wiese W L, Smith M W and Glennon B M 1996 *Atomic Transition Probabilities. Vol. 1. Hydrogen through Neon (US National Bureau of Standards National Standard Reference Series, Washington, DC NSRDS-NBS)*

[20] Spence T G, Xie J, Zare R N, Packan D M, Yu L, Laux C O, Owano T G and Kruger C H 1999 Cavity ring-down spectroscopy measurements of N_2^+ in atmospheric pressure air plasmas *AIAA 99-3433, 30th AIAA Plasmadynamics and Lasers Conf. (Norfolk, VA)*

[21] Yalin A P, Laux C O, Kruger C H and Zare R N 2002 Spatial profiles of N_2^+ concentration in an atmospheric pressure nitrogen glow discharge *Plasma Sources Sci. Technol.* **11** 248–53

[22] Yalin A P, Zare R N, Laux C O and Kruger C H 2002 Temporally resolved cavity ring-down spectroscopy in a pulsed nitrogen plasma *Appl. Phys. Lett.* **81** 1408–10

[23] O'Keefe A and Deacon D A G 1988 Cavity ring-down optical spectrometer for absorption measurements using pulsed laser sources *Rev. Sci. Instrum.* **59** 2544–51

[24] Zalicki P and Zare R N 1995 Cavity ring-down spectroscopy for quantitative absorption measurements *J. Chem. Phys.* **102** 2708–17

[25] Siegman A E 1986 *Lasers* (Mill Valley: University Science Books)

[26] Elleaume P, Velghe M, Millardon M and Ortega J M 1985 Diagnostic techniques and UV-induced degradation of the mirrors used in the Orsay storage ring free-electron laser *Appl. Opt.* **24** 2762

[27] Martin J, Paldus B A, Zalicki P, Wahl E H, Owano T G, Harris J S, Kruger C H and Zare R N 1996 Cavity ring-down spectroscopy with Fourier-transform-limited light pulses *Chem. Phys. Lett.* **258** 63–70

[28] Yalin A P and Zare R N 2002 Effect of laser lineshape on the quantitative analysis of cavity ring-down signals *Laser Phys.* **12** 1065–72